*Article*

# Synthesis and Characterization of Polystyrene-Montmorillonite Nanocomposite Particles Using an Anionic-Surfactant-Modified Clay and Their Friction Performance

**Chengcheng Yu** [iD], **Yangchuan Ke \***, **Qingchun Deng, Shichao Lu, Jingqi Ji, Xu Hu and Yi Zhao**

Nanotechnology Center of Energy Resources, CNPC Nanochemistry Key Laboratory, College of Science, China University of Petroleum, Beijing 102249, China; yccycc9999@163.com (C.Y.); qcdeng2014@163.com (Q.D.); lushichao1@126.com (S.L.); jjq8907@163.com (J.J.); HuXu910203@163.com (X.H.); dzhaoyi2015@163.com (Y.Z.)
**\*** Correspondence: kyc010@sohu.com

check for updates

**Abstract:** Polystyrene-organo-montmorillonite (PS-OMMT) nanocomposite particles were prepared via emulsion polymerization of styrene in the presence of montmorillonite modified with an anionic surfactant, sodium lauryl sulfonate (SLS), and its tribological properties as an additive to polyalphaolefin (PAO) were tested. The results of Fourier transform infrared spectroscopy (FT-IR), X-ray diffraction (XRD) and thermogravimetric analysis (TGA) showed that SLS molecules resided in the montmorillonite (MMT) interlayer space. The effects of OMMT on the morphology and properties of the nanocomposites were also investigated. Gel permeation chromatography (GPC) and dynamic light scattering (DLS) demonstrate that the presence of OMMT can effectively reduce the average molecular weight and average particle size of PS. XRD and transmission electron microscopy (TEM) of the PS-OMMT nanocomposites indicate that exfoliated and intercalated structures form and that the MMT layers either are partly embedded inside the PS particles or remain on their surface. Compared with pure PS, the PS-OMMT nanocomposites possessed higher stability to thermal decomposition and higher glass transition temperatures. Adding nanocomposite particles reduces the friction coefficient, and thus, the antiwear properties of the PAO are significantly improved. The PS-OMMT-3 (3 wt % of OMMT based on styrene) particles have the best tribological performance and maintained a stable, very low coefficient of friction of 0.09.

**Keywords:** organoclay; emulsion polymerization; nanoparticles; morphology; tribological property

## 1. Introduction

Recently, polymer-clay nanocomposites have attracted considerable interest from researchers due to their tremendous properties and broad applications [1–5]. By introducing a low clay content (usually 1–10 wt %) into a polymer matrix, these nanocomposites can achieve many unique properties, such as reduced thermal diffusion coefficients, increased barrier characteristics, high heat-distortion temperatures, decreased gas permeability and enhanced mechanical properties, compared with conventional composites or pure polymers [6–9]. The factors impacting the efficiency of these nanocomposite materials include the aspect ratio of the clay layers, the dispersion quality and the interfacial adhesion between the polymer matrix and the clay layers [10,11]. Unique and improved properties are often observed when the dispersed clay layers were less than 100 nm thick. Thus, many techniques have been evaluated to achieve homogeneous dispersions of ultrafine silicate clay layers inside polymer matrices. Layered silicates such as sodium-montmorillonite (MMT), which is an aluminosilicate mineral with sodium counterions between its layers, are one of the types of materials

most commonly used for making polymer-based nanocomposite inorganic materials because of their high aspect ratios, large specific surface areas, high cation exchange capacities and excellent swelling capacities [12,13]. In an MMT crystal structure, the two-dimensional layers are formed by the fusion of a central octahedral sheet of alumina with the tips of two external silica tetrahedra, and the sheet thickness is approximately 1.00 nm [14]. Due to the incompatibility of the hydrophilic MMT surface with the hydrophobic polymer matrix, the individual layers are not easily separated and dispersed in most organic polymers [15]. Therefore, to improve the affinity of these clay layers for organic polymers, the clay layers are usually treated with surfactants to increase their hydrophobicity for the synthesis of clay-based nanocomposites [12]. The surfactants can not only improve the compatibility between the clay layers and the polymer matrix but also enlarge the interlayer gallery spaces of the clay, which is significant for allowing monomers to penetrate into the clay galleries and to polymerize.

Conventional MMT modifiers include quaternary ammonium cationic surfactants, from which many products have been commercialized over the past few decades. Chen et al. prepared an organic montmorillonite with cetyltrimethylammonium bromide (CTAB) by a cationic exchange reaction and synthesized exfoliated PS-MMT nanocomposites containing 5 wt % CTAB-MMT [16]. Simons and coworkers employed a series of quaternary ammonium surfactants as clay modifiers to investigate the impact of the chemical structure of the surfactant on the morphology of the PS-MMT nanocomposites prepared via bulk polymerization [17]. Zhu et al. prepared organic montmorillonite by anchoring two functionalized ammonium salts inside the MMT interlayer galleries to investigate the fire resistance of the respective intercalated and exfoliated PS-clay nanocomposites [18]. However, MMT modified with conventional cationic surfactants has a fundamental problem: the quaternary ammonium surfactants decompose at temperatures above 170–180 °C. Therefore, MMT modified by traditional cationic ammonium surfactants is not suitable for high-temperature processes and applications. For these reasons, MMT modified by an anionic surfactant was designed and prepared due to the excellent thermal stability of anionic surfactants compared to traditional cationic surfactants [19]. Furthermore, the swelling, thixotropy and dispersion properties of MMT modified by an anionic surfactant are superior to those of CTAB-modified MMT [19]. Nevertheless, reports on anionic surfactant-modified MMT account for <20% of all reported MMTs, and only a few reports have considered MMT modification using anionic surfactants for the synthesis of polymer-clay nanocomposites [20].

Polystyrene (PS) is a thermoplastic material that is suitable for versatile applications in the engineering and coatings fields [21]. However, the thermal stability of PS is a key factor in determining its suitability for a particular application. Layered silicates possess relatively high thermal stabilities. Therefore, the formation of PS and MMT nanocomposites could compensate for the relatively low stability of PS such that the resulting material could have more extensive applications in high-temperature processes. Several methods have been applied for the preparation of polymer-clay nanocomposites, such as bulk polymerization, solution polymerization, emulsion polymerization and the melt-intercalation method [22–25]. Among these methods, emulsion polymerization was considered the most promising technique for the fabrication of monodispersed polymer nanoparticles with controlled molecular weights, faster reaction rates, and improved environmental friendliness because water is used as the reaction solvent. Moreover, emulsion polymerization facilitates the preparation of exfoliated structures in polymer-MMT composites. Zhang et al. prepared mono-disperse silica-polymer core-shell microspheres via emulsion polymerization [26]. In addition, Li et al. synthesized exfoliated PS-MMT nanocomposites by emulsion polymerization using zwitterions as the clay modifier, and these nanocomposites showed improvements in thermal stability compared with intercalated composites and the neat polymer [27]. Wang et al. observed that ultrasound or ultrasonic irradiation processes assisted emulsion polymerization and could promote the formation of exfoliated layers during nanocomposite synthesis [28]. In addition, the results of Yang et al. indicated that PS-clay nanocomposites synthesized via emulsion polymerization had better layer dispersion than those synthesized by suspension polymerization [29]. Therefore, emulsion polymerization is

an efficient technique for preparing polymer-MMT nanocomposite particles with exfoliated structures and monodispersity.

In this paper, we report the effect of anionic surfactant modifiers on MMT and discuss a possible mechanism of the effect of the anionic surfactant in the intercalated MMT. The PS-OMMT nanocomposite particles were prepared via emulsion polymerization, and the effects of OMMT on the morphology, structure, and thermal properties of the polystyrene matrix were investigated. In addition, the tribological properties of PS-OMMT nanocomposite particles as additives in polyalphaolefin (PAO) were investigated. The results showed that these nanocomposite particles were effective friction reduction and antiwear materials and could have applications in oil and gas drilling engineering to improve drilling fluid lubrication. Further work in this direction is currently in progress.

## 2. Materials and Methods

### 2.1. Materials

Sodium montmorillonite (MMT) with a cationic exchange capacity (CEC) of 100 meq/100 g of clay was purchased from Huai An Saibei Technology Co. Ltd. (Huaian, China). Styrene (St, >98%) monomer and divinylbenzene (DVB, >80%) were obtained from the Tianjin Guangfu Fine Chemicals Research Institute (Tianjin, China) and were distilled under reduced pressure before use. Sodium lauryl sulfonate (SLS, 99%, AR) and potassium persulfate (KPS, 99%, AR) were purchased from Beijing Chemical Reagents Company (China). Polyalphaolefin (PAO, 99% purity) was purchased from Shanghai Fox Chemical Technology (China). All other reagents were of analytical grade and were purchased from the Tianjin Guangfu Fine Chemicals Research Institute (China), and were used without further purification. Deionized water was used throughout the experiments.

### 2.2. Preparation of OMMT

OMMT was prepared by a modified process based on a typical purification and separation process [30]. The OMMT preparation process is depicted in Figure 1 (Stage A). For the preparation of OMMT, MMT (2.5 g) was dispersed in 75.0 mL of deionized water in a three-neck flask (500 mL), and the dispersion was stirred vigorously for 30 min at room temperature. The pH of the suspension was adjusted to 1 using a certain amount of hydrochloric acid, and the mixture was heated to 80 °C for 30 min with vigorous stirring. Then, a solution of SLS in 25.0 mL of deionized water was slowly added to the clay suspension under continuous stirring. The amount of SLS was equivalent to 1.2 CEC of MMT. After reacting for 9 h, the resulting sample was separated by filtration and thoroughly washed with boiling deionized water until the pH of the supernatant solution was approximately 7. The final products were then dried overnight at 60 °C in a vacuum oven, ground with a mortar and pestle, and sieved with the 200-mesh sieve for further use.
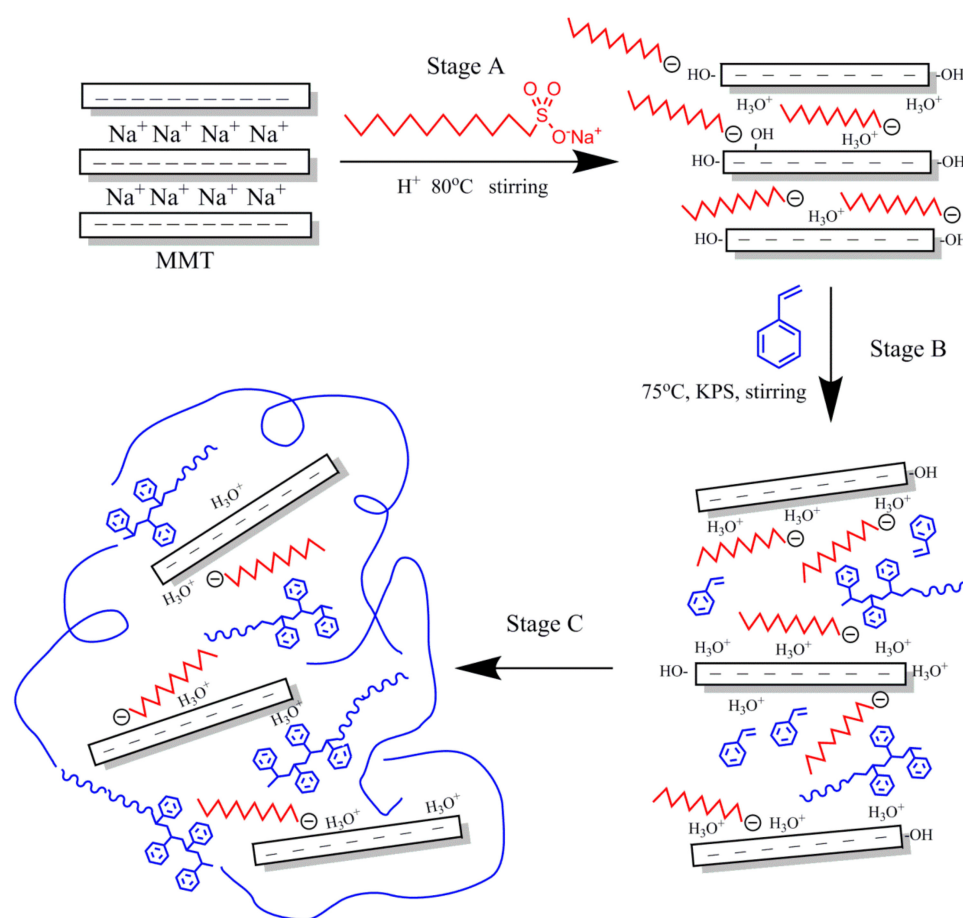
**Figure 1.** Proposed reaction mechanism for the synthesis of PS-OMMT nanocomposites.

## 2.3. Preparation of PS-OMMT Nanocomposites

Emulsion polymerization was applied to the synthesis of the PS-OMMT nanocomposite particles via a previously reported procedure with slight modifications [31]. As shown in Figure 1 (Stages B,C), the surfactant SLS (0.36 g) was dissolved in 100.0 mL of deionized water in a 500 mL three-neck flask at room temperature with continuous stirring. Thereafter, a certain amount of OMMT was dispersed in the mixture of styrene (20.0 mL) and divinylbenzene (2.0 mL) at room temperature for 1 h to allow the OMMT to become completely swollen. Then, the suspension of OMMT was added to the reactor with continuous stirring at 75 °C for 30 min to ensure homogenization of the inorganic and organic phases under a nitrogen atmosphere. Finally, KPS initiator (0.072 g) was added to the mixture, and the system was reacted with stirring for 8 h. After the end of the reaction, the demulsification process was carried out with ethanol, and the obtained samples were washed and purified three times using excess hot ethanol to remove any unreacted monomer and oligomers, followed by filtration. The final products were dried under reduced pressure in a vacuum oven at 60 °C for 24 h, prior to characterization. The nanocomposites prepared with 1, 3, and 5 wt % (based on the weight of styrene) OMMT loadings were designated PS-OMMT-1, PS-OMMT-3, and PS-OMMT-5, respectively. For comparison, pure PS was synthesized according to the method described above.

## 2.4. Preparation of PAO-PS-OMMT Lubricant

To test the tribological performance of the PS-OMMT nanocomposite particles as additives, 1 wt % (based on the weight of PAO) of PS-OMMT samples were dispersed in PAO with rapid stirring. After that, the mixture was ultrasonicated for 1 h to form a homogeneous solution in PAO.

*2.5. Characterization*

Fourier transform infrared (FTIR) spectra of the samples were obtained using an FTS-3000 spectrophotometer (Digilab, Cambridge, MA, USA) within the range of 4000–400 cm$^{-1}$ at room temperature. The powder samples were characterized by a KBr pressed disk technique with a weight ratio of the sample to KBr of 1/100.

X-ray diffraction (XRD) patterns were obtained on a Bruker D8 Advance X-ray Diffractometer (STADI P, Karlsruhe, Germany) with Cu-Ka radiation ($\lambda$ = 0.1540 nm) at a scan rate of 2°/min from 1.5° to 20° with a step distance of 0.02°. The basal spacing reflections of the samples were calculated from Bragg's Law, and the voltage and current of the X-ray tubes were 40 kV and 30 mA, respectively.

The molecular weight and molecular weight distribution were characterized by a gel permeation chromatography system (GPC515-2410, Waters, Milford, MA, USA) equipped with a 2410 Refractive Index Detector and a 996 Photodiode Array Detector using tetrahydrofuran (THF) as an eluent at a flow rate of 1.0 mL/min. The molecular weight calibration curve was obtained using polystyrene standards.

The particle size and size distribution of the samples were determined by dynamic light scattering using a Malvern Mastersizer 2000 (Malvern Instruments, Malvern, UK) at 25 °C.

Scanning electron microscopy (SEM, SU8010, HITACHI, Tokyo, Japan) was used to observe the surface morphology of the samples with an accelerating voltage of 15 kV after coating the samples with thin layers of gold.

The dispersion morphology of the clay layers in the polymer matrix was obtained using transmission electron microscopy (TEM, JEM-2100, Tokyo, Japan) with an accelerating voltage of 200 kV.

The weight losses of the samples were determined using a NETZSCH thermogravimetric analyzer (TGA, STA409PC, Bavaria, Germany). The samples were between 2.0 and 5.0 mg and were heated from 25 °C to 800 °C at a heating rate of 10 °C/min under $N_2$ at a flow rate of 140 cm$^3$/min.

The glass transition temperature of PS/OMMT was obtained by using differential scanning calorimetry (DSC, 6220, Japan) at a heating rate of 10 °C/min under $N_2$ at a flow rate of 100 cm$^3$/min.

The tribological properties of the PS/OMMT samples were tested using an MRS-1J four-ball tester. GCr15 steel bearing balls with a 12.7 mm diameter (grade 10) were cleaned ultrasonically with ethanol before the test. All the tests were performed at a rotating speed of 1450 r/min for 60 min under a load of 392 N at room temperature. The coefficient of friction (COF) was recorded three times, and the average COF values were calculated.

## 3. Result and Discussion

*3.1. Fourier Transform Infrared Spectroscopy*

Figure 2 shows the infrared spectra of MMT (A), OMMT (B), PS (C) and PS-OMMT-3 (D). In Figure 2A, for the MMT sample, the absorption bands at 3446.4 cm$^{-1}$ and 1643.4 cm$^{-1}$ correspond to -OH stretching vibrations and H-O-H bending vibrations of the MMT interlayer water molecules, respectively. The characteristic adsorption bands at 3632.5 cm$^{-1}$ and 1036.1 cm$^{-1}$ were attributed to the Al (Mg)-OH bending vibrations and Si-O stretching vibrations, respectively. The characteristic band at 798.6 cm$^{-1}$ corresponds to the Si-O-Al stretching vibrations. In contrast, for the OMMT sample spectrum shown in Figure 2B, the characteristic adsorption bands at 2925.6 cm$^{-1}$ and 2860.2 cm$^{-1}$ respectively correspond to the asymmetric -CH$_2$ and symmetric -CH$_2$ stretching vibrations in the SLS molecular chain. In addition, the adsorption band at 1185.5 cm$^{-1}$ corresponds to an -SO$_3$H asymmetric stretching vibration. Moreover, compared with those of MMT, the absorption bands at 3440.3 cm$^{-1}$ and 1632.7 cm$^{-1}$ of the OMMT weaken and shift to a lower wavenumber, which indicates that the water content in OMMT is reduced with the SLS modification. These observations indicate that the anionic surfactant molecules are present on the surface or intercalated into the interlayer spaces of the MMT. In Figure 2C, PS showed strong bands at 3027.9–3100.5 cm$^{-1}$ and 2850.3–2920.6 cm$^{-1}$, corresponding to CH aromatic stretching vibrations and CH$_2$ asymmetric stretching vibrations, respectively. There are two absorption bands at 1603.5 cm$^{-1}$ and 1447.1–1503.4 cm$^{-1}$ that correspond

to absorptions from aromatic C=C stretching vibrations. The adsorption bands at 758.7 cm$^{-1}$ and 698.1 cm$^{-1}$ represent the C–H out-of-plane bending vibrations. In addition, the absorption band at 3449.2 cm$^{-1}$ corresponds to an absorption from O–H stretching vibrations, indicating the presence of hydroxyl groups. These observations suggest that the polymerization reaction of St has occurred. Compared with PS, PS-OMMT-3 clearly shows a characteristic adsorption band at 1043.9 cm$^{-1}$, which corresponds to the Si-O stretching vibrations in OMMT. The FTIR spectrum of PS-OMMT-3 contains the adsorption band corresponding to OMMT, confirming the inclusion of montmorillonite in the PS matrix.
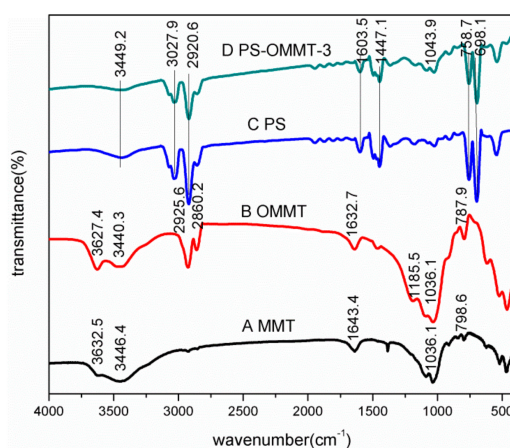


**Figure 2.** FTIR spectra of (**A**) MMT, (**B**) OMMT, (**C**) PS and (**D**) PS-OMMT-3.

### 3.2. X-Ray Diffraction

The XRD patterns of MMT, OMMT, PS, PS-OMMT-1, PS-OMMT-3 and PS-OMMT-5 are shown in Figure 3A–F, respectively. As shown in Figure 3A, a typical MMT diffraction peak appeared at 2θ = 7.28°, corresponding to a basal interlayer distance of 1.21 nm according to Bragg's law. After modification by SLS, as shown in Figure 3B, the diffraction peak of OMMT shifted to 2θ = 5.79°, suggesting that the interlayer distance had increased to 1.52 nm. This result indicated that the anionic surfactant molecules were successfully intercalated into the MMT interlayer spaces, thereby expanding the interlayer distance and causing the surface properties of MMT to change from hydrophilic to hydrophobic.
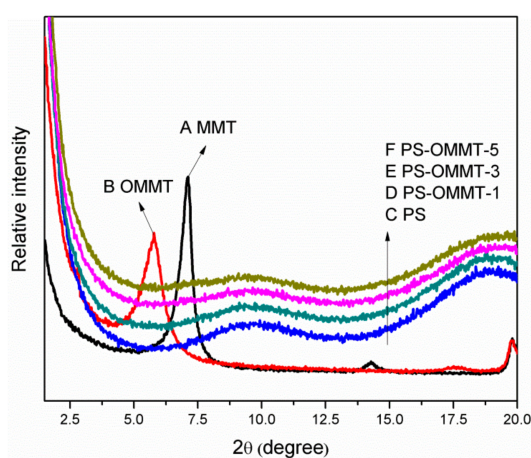


**Figure 3.** X-ray diffraction patterns of (**A**) MMT, (**B**) OMMT, (**C**) PS, (**D**) PS-OMMT-1, (**E**) PS-OMMT-3 and (**F**) PS-OMMT-5.

However, there is currently no universal understanding of the mechanism for the intercalation of an anionic surfactant into MMT. Zhang proposed that the intercalation of the anionic surfactant was due to the formation of ion pairs between the surfactant anions and hydronium ions or $Na^+$ and $Ca^{2+}$ counterions and that these ion pairs then entered the interlayer spaces in different arrangements [19]. However, the isomorphous substitution of $Mg^{2+}$ for $Al^{3+}$ or, rarely, $Al^{3+}$ for $Si^{4+}$ generates a net negative charge on the surface of MMT layers [32]. Furthermore, many hydroxyl groups are present at the edges of MMT, and few are present on the external and internal surfaces due to electrostatic interactions with hydronium ions. In addition, in acidic media, the negative charge density on the MMT surface will decrease, and the number of hydroxyl groups will increase because a large concentration of hydronium ions enter the interlayer space of the MMT [19]. Therefore, the anionic surfactant could generally intercalate into the MMT interlayer spaces through the replacement of or interaction with hydroxyl groups at the MMT layer edges (see stage A in Figure 1). As surfactants are inserted into the clay layers, the electrostatic repulsion between the layers gradually increases, resulting in an increase in the spacing between the clay layers. Thus, the anionic surfactant transforms MMT to OMMT with enlarged interlayer spacing, into which the styrene monomer can easily enter and polymerize.

As shown in Figure 3C–F, the disappearance of the MMT diffraction peaks in these patterns indicated that the PS chains were inserted into the OMMT gallery, which is the interlayer space of OMMT, and destroyed the ordered clay structure during the emulsion polymerization process. In the PS-OMMT nanocomposites, no OMMT diffraction peaks were visible because the OMMT tactoids were likely exfoliated and dispersed in a disorderly fashion into the PS matrix at the molecular level or because the clay interlayer distances were greater than 6 nm [33]. However, the absence of XRD peaks does not necessarily indicate complete exfoliation of the clay layers [34]. Thus, the dispersion and degree of exfoliation of the clay layers, as well as the microstructure morphology in the matrix, were further corroborated by TEM analysis. TEM micrographs of the PS and nanocomposite samples are shown in Figure 4.

### 3.3. Transmission Electron Microscopy

In the TEM images, the dark lines represent the clay layers, and the brighter regions represent the polymer matrix. Figure 4A shows that the pure PS particles were transparent spheres with diameters of approximately 130 nm. In contrast, in Figure 4B–D, the clay layers appear to have an exfoliated and/or intercalated arrangement with good dispersion in the polymer matrix. Meanwhile, in Figure 4B,C, mainly exfoliated structures (marked by yellow arrows) were seen in the PS matrix, indicating a high degree of exfoliation and dispersion of the clay layers in the matrix. Furthermore, some individual clay layers appeared to be either located on the surface of the PS particles or partially embedded inside the PS particles as the OMMT load increased to 3 wt %. This morphology was also observed by other researchers [35]. In appropriate amounts (1–3 wt %), the OMMT can be effectively exfoliated to form individual layers due to the strong interactions between the OMMT and the polymer matrix. However, with an increase in the clay content, many intercalation structures (marked by red ellipses) were observed, as shown in Figure 4D. This result suggested that excess OMMT can lead to ineffective exfoliation and the appearance of heterogeneous stacks of clay layers due to adhesion of the nanostructures. Furthermore, all the PS-OMMT nanocomposite samples appeared to have particle sizes smaller than pure PS. This decrease in the size of the nanocomposite particles can be attributed to the increased dispersion of clay in the PS matrix and the increase in SLS concentration, resulting in the formation of more surfactant micelles.
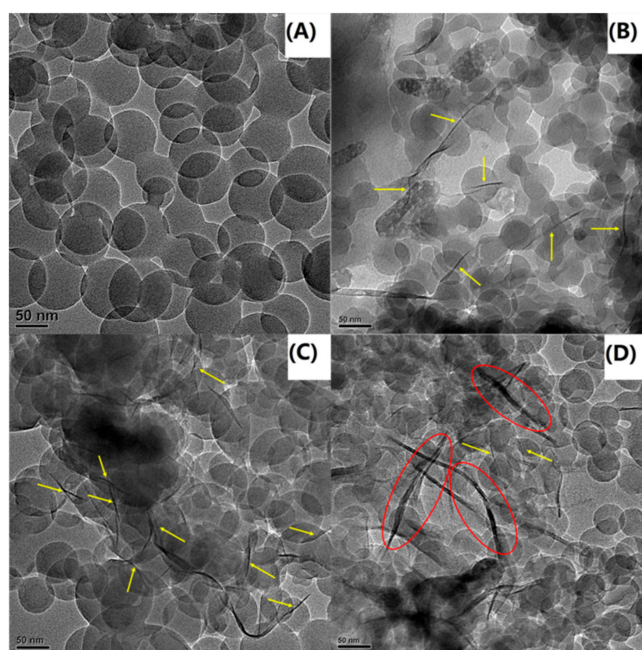
**Figure 4.** TEM images of (**A**) PS, (**B**) PS-OMMT-1, (**C**) PS-OMMT-3 and (**D**) PS-OMMT-5.

### 3.4. Gel Permeation Chromatography

The molecular weight data and the impact of OMMT on the molecular weight of the PS-OMMT nanocomposite samples are summarized in Table 1.

From Table 1, it can be seen that the number-average molecular weight ($M_n$) and the weight-average molecular weight ($M_w$) of the PS-OMMT nanocomposite samples decreased significantly compared with those of pure PS. This result was attributed to the MMT layers hindering diffusion of the monomer and/or polymer chain growth [36–38]. Interestingly, both the lowest molecular weight and polydispersity index (PDI) values were seen in the PS-OMMT-3 sample. This result was ascribed to the better exfoliation and higher dispersion of clay layers in the PS-OMMT-3 sample, leading to an increase in the diffusion path of the monomer and a decrease in polymer chain growth. However, as the clay content was increased, the $M_n$, $M_w$ and PDI of the PS-OMMT-5 sample increased. This result is attributed to the reduction in the exfoliated structures and the increase in the number of agglomerates in the PS-OMMT-5 samples, resulting in a poor barrier effect of the clay layers and thus favoring polymer chain growth and increase of the molecular weights.

**Table 1.** Molecular weight distribution of PS and PS-OMMT nanocomposites.

| Sample Code | $M_n$ ($\times 10^5$) | $M_w$ ($\times 10^5$) | PDI |
|:---:|:---:|:---:|:---:|
| PS | 3.65 | 15.09 | 4.14 |
| PS-OMMT-1 | 1.76 | 7.56 | 4.31 |
| PS-OMMT-3 | 1.56 | 5.57 | 3.57 |
| PS-OMMT-5 | 1.55 | 7.35 | 4.74 |

### 3.5. Thermal Stability

Thermogravimetric analysis (TGA) measurements of the MMT and OMMT samples are shown in Figure 5. As shown in Figure 5, at temperatures below 100 °C, the mass losses of the MMT and OMMT samples arising from the dehydration of water molecules adsorbed on the clay surfaces and the interlayer spaces were 7.1% and 5.0%, respectively. Moreover, the water content of OMMT was less than that of MMT, which indicated that the absorbed water molecules were partially replaced by the

anionic surfactant. During this stage, the SLS molecules were intercalated into the interlayer spaces of the MMT, resulting in a change from a hydrophilic MMT surface to a hydrophobic one. The MMT mass loss in the temperature range of 100–800 °C, corresponding to dehydroxylation of the MMT, was merely 5.3%, [34]. The total MMT mass loss was approximately 12.4%. In contrast, there was an obvious mass loss in the temperature range of 350–500 °C for the OMMT samples, which was attributed to the evaporation/decomposition of the loaded anionic surfactants, such that the mass loss reached approximately 11.4%. In the temperature range of 500–800 °C, the OMMT mass loss arising from dehydroxylation of the MMT layers was approximately 5.3% [34]. The total mass loss of OMMT was approximately 24.0%. As shown above, the total amount of anionic surfactants in the OMMT was close to 70% of mole percent based on the CEC value (i.e., 100 mmol/100 g clay). This result further confirmed that the anionic surfactant was indeed intercalated into the MMT interlayers, as previously indicated by the XRD patterns shown in Figure 3.
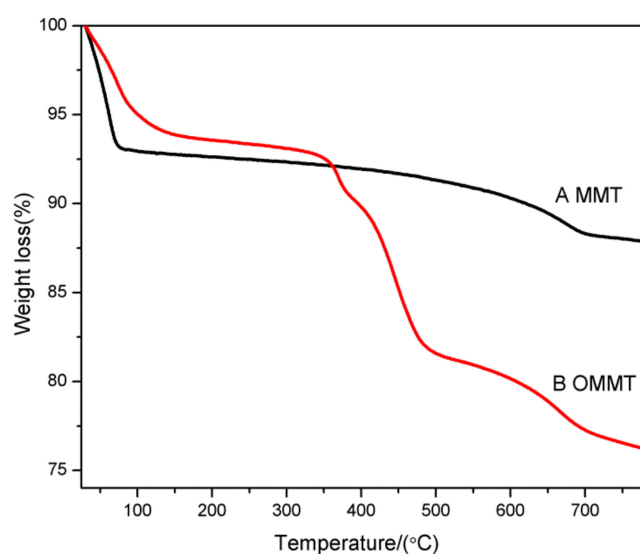


**Figure 5.** TGA curves of (**A**) MMT and (**B**) OMMT.

Figure 6 presents TGA traces and derivative thermogravimetry (DTG) results for the pure PS and PS-OMMT nanocomposites. In Figure 6, the nanocomposites showed similar degradation behaviors (curve patterns) as the pure polymer, indicating a similar degradation mechanism to pure PS. Figure 6 shows that the onset degradation temperature ($T_{10}$, 10 wt % mass loss) increased from 346.1 °C for pure PS to 348.7 °C, 376.2 °C and 372.8 °C for the PS-OMMT-1, PS-OMMT-3 and PS-OMMT-5 samples, respectively. The temperatures of the maximum decomposition rate ($T_{max}$), as revealed by the DTG curves, followed the same trend and increased by 6.7 °C, 18.1 °C and 13.0 °C, respectively, compared with pure PS. These results suggested that the introduction of OMMT improved the thermal stability of the polystyrene, which may be attributed to a labyrinth or barrier effect originating from the high aspect ratio of the clay layers, which can prevent diffusion of the volatile decomposition products out of the polymer in the thermal degradation zone [39]. However, PS-OMMT-3 was found to have the best thermal stability and a 30.1 °C enhancement in the onset degradation temperature over pure PS. Furthermore, the best enhancement in the $T_{max}$ was also achieved in the PS-OMMT-3 sample. These results were attributed to the higher degree of exfoliation of the clay layers and better dispersion obtained in the PS-OMMT-3 sample than the other samples. It was plausible that the exfoliated and dispersed clay layers played a significant role as nucleating agents in the polymer matrix by limiting the heat transfer, which may enhance the degradation temperature [31]. In addition, the improvements in thermal stability are related to the relatively strong interfacial interactions between the clay layers and the polymer chains for the PS-OMMT-3 sample due to existence of a large number of OMMT

single layers [40]. Meanwhile, the insufficient number of clay layers caused the presence of a barrier at low OMMT loadings (PS-OMMT-1) that could act as thermal insulators and enhance the thermal properties of the materials, although exfoliated structures are favorable at low OMMT contents. However, a slight decrease in $T_{10}$ and $T_{max}$ was observed in the PS-OMMT-5 sample. Excessive OMMT aggregation might have destroyed the effective dispersion and interaction between the clay layers and the PS matrix, resulting in a lower thermal stability [41]. Therefore, the thermal stability of the PS-OMMT nanocomposite was not only dependent on the clay loading but also closely related to the clay dispersion and degree of exfoliation, and the interactions between the OMMT and PS matrix also played an important role in improving the thermal performance [42,43].
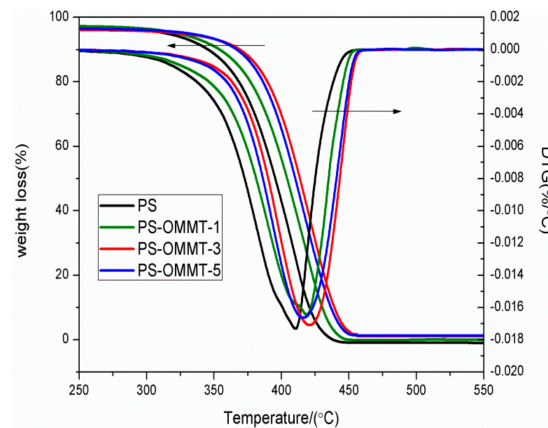


**Figure 6.** TGA and DTG curves of PS, PS-OMMT-1, PS-OMMT-3 and PS-OMMT-5.

### 3.6. Differential Scanning Calorimetry

The thermal behaviors of pure PS and PS-OMMT nanocomposites were further investigated with DSC (Figure 7).

As shown in Figure 7, the glass transition temperature ($T_g$) of all the nanocomposites increased relative to the pure PS. This fact indicated that the clay layers can improve the $T_g$ of the PS matrix by limiting the segmental motion of the polymer chains. PS-OMMT-3 showed the optimal increase in $T_g$, increasing by 3.9 °C compared to pure PS (124.7 °C). This was due to the higher degree of exfoliation and better dispersion of the clay layers, which could effectively confine the thermal motion of the polymer chains [44]. However, at a 5 wt % OMMT loading, the $T_g$ values of the samples would decrease slightly, probably due to the formation of more clay agglomerates that could not effectively impede the movement of the PS chains.
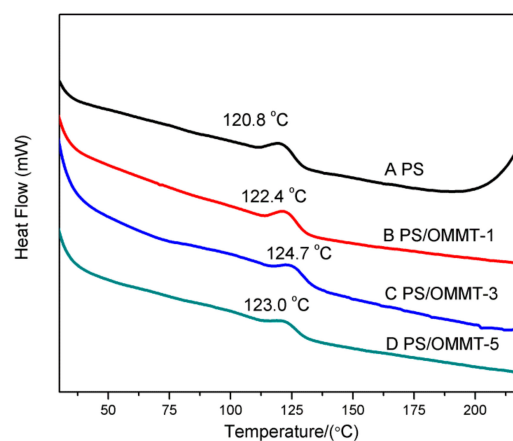


**Figure 7.** DSC curves of (**A**) PS, (**B**) PS-OMMT-1, (**C**) PS-OMMT-3 and (**D**) PS-OMMT-5.

### *3.7. Particle Size Analysis*

The particle sizes and size distributions of the pure PS and its nanocomposite samples are shown in Figure 8. Table 2 summarizes the average particle size data and PDI values. As shown in Figure 8, for pure PS, a unimodal and relatively broad particle size distribution was observed, and the average particle diameter was approximately 129.5 nm. However, in the case of the PS-OMMT nanocomposite samples, the particle distributions were narrower, and the average particle diameters were in the range of 62.83–64.58 nm. The PDI values of PS, PS-OMMT-1, PS-OMMT-3 and PS-OMMT-5 samples were 0.204, 0.082, 0.079 and 0.102, respectively. The particle sizes of pure PS and the nanocomposite samples were also confirmed by the TEM images, as shown in Figure 4. These results indicated that a certain OMMT load (<5 wt %) could decrease the particle size diameter and improve the monodispersity of the particles. The OMMT layers might act as nucleating agents to form smaller and more uniform nanoparticles during the polymerization process [45]. However, the minimum average particle size and PDI values were achieved in the samples containing 3 wt % OMMT loading. This was because of the higher degree of exfoliation and better dispersion of the clay layers in PS-OMMT-3 could more effectively impede the movement of the styrene monomers and increase the concentration of SLS to form the finer and more stable emulsion, which lead to reduction in the size of nanocomposite particles. As shown in Figure 8 and Table 2, however, the difference in the particle size of the three clay containing samples is not significant. In other words, the three clay containing samples are equal with respect to particle size, considering the error in the measurement.
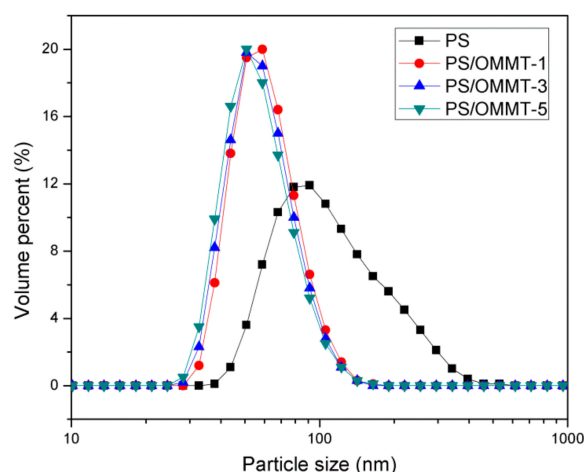


**Figure 8.** Particle size distribution curves of PS, PS-OMMT-1, PS-OMMT-3 and PS-OMMT-5.

**Table 2.** Particle size distribution of PS and PS-OMMT nanocomposites.

| Sample Code | Z-Average (nm) | PDI |
|:---:|:---:|:---:|
| PS | 129.5 ± 6.5 | 0.204 |
| PS-OMMT-1 | 64.58 ± 2.91 | 0.082 |
| PS-OMMT-3 | 62.83 ± 2.19 | 0.079 |
| PS-OMMT-5 | 63.38 ± 2.92 | 0.102 |

### *3.8. Scanning Electron Microscopy*

Direct observations of the size and size distribution of the nanocomposites were made via SEM analysis. As observed in Figure 9A, the pure PS particles were spherical with a very smooth surface and a particle size diameter of approximately 120 to 140 nm. In contrast, the PS-OMMT nanocomposites (Figure 9B–D) showed spherical particles with obviously decreased diameters of approximately 60 to 70 nm. These results were in agreement with the results shown Figures 4 and 8. Furthermore, relatively smooth particle surfaces were obtained, and a certain degree of adhesion

between these particles was also observed due to the MMT layers located either on the surface or partially embedded inside the PS particles, as shown in Figure 4. This particle morphology indicated that the OMMT played a significant role in the formation of nucleation centers during the process of emulsion polymerization, thereby restricting particle growth. However, as the amount of clay increases (above 5 wt %), the clay layers agglomerate and form intercalated structures, leading to an increase in the particle size and PDI.
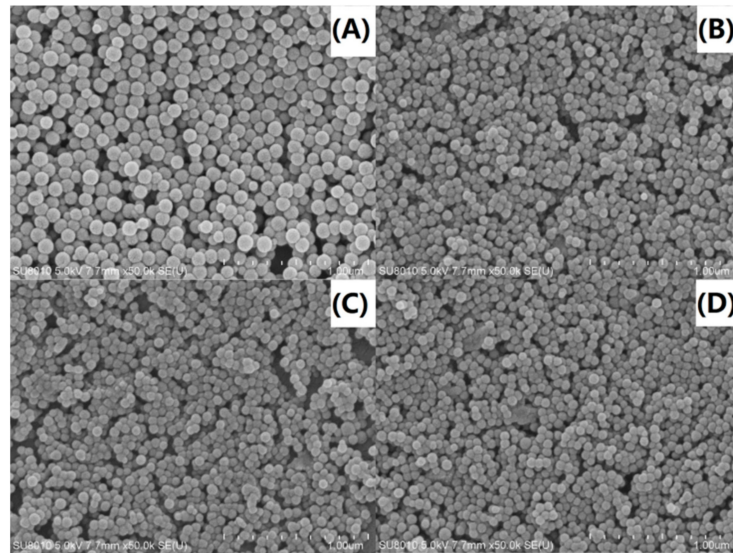


**Figure 9.** SEM images of (**A**) PS, (**B**) PS-OMMT-1, (**C**) PS-OMMT-3 and (**D**) PS-OMMT-5.

### 3.9. Friction Performance Analysis

The coefficient of friction (COF) versus the experiment time for PAO and PAO with 1 wt % (based on the weight of PAO) of the PS-OMMT nanocomposite samples is shown in Figure 10.

In Figure 10, the COF of PAO initially was approximately 0.10. However, it subsequently increased to approximately 0.14 within 500 s and then experienced a stable period of time between approximately 500 s and 700 s. The COF then decreased slightly from 0.14 to approximately 0.13 within 2500 s, followed by an increase to 0.15 with fluctuations. However, for the PAO-PS-OMMT nanocomposites, the COF values were clearly decreased compared with those of PAO because when the PS-OMMT nanocomposite particles were taken into the contact area by the lubricant, they were likely to support the two counterparts and prevent them from contacting each other and rolling like bearing ball in bearing between two metal surfaces to reduce the COF value. For the PAO-PS-OMMT-1 sample, the COF increased with fluctuations from 0.08 at the beginning to 0.11 until approximately 2000 s and then remained relative steady for the rest of the test. For the PAO-PS-OMMT-3 sample, the COF started at 0.078 and increased to approximately 0.095 within 500 s. It then remained relatively stable, and at the end of the test, the COF was approximately 0.09. For the PAO-PS-OMMT-5 sample, the COF increased sharply from 0.083 to approximately 0.10 near 300 s and then increased slowly to approximately 0.12 at the end of the test. It could be found that with the same content of nanocomposite particles, PAO-PS-OMMT-3 demonstrated the best friction reduction and the lowest COF value. This result indicated that the PS-OMMT-3 nanocomposite particles with a higher degree of exfoliation and better dispersion of MMT can effectively support the two counterparts and prevent contact more efficiently than the other studied materials.
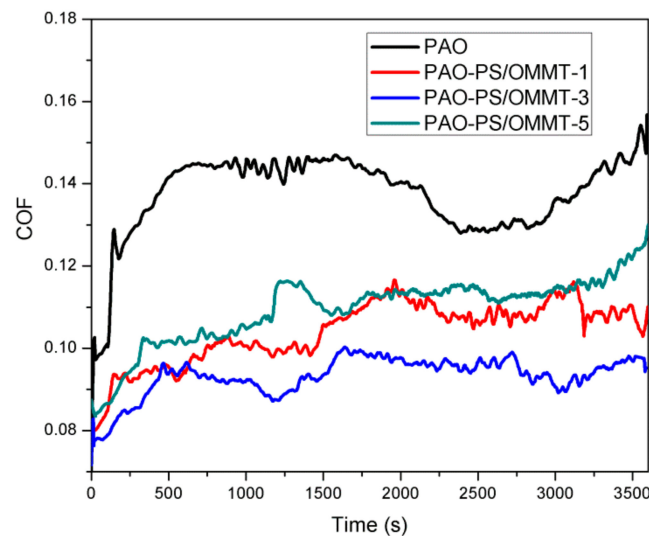
**Figure 10.** The COF versus time of PAO and PAO-PS-OMMT nanocomposites.

To further investigate the variations in the tribological behavior due to the addition of the PS-OMMT nanocomposite particles, the wear surface morphologies of PAO and the nanocomposites were examined by SEM. SEM images of the wear surfaces of the upper and lower ball of the four-ball machine for PAO, PAO-PS-OMMT-1, PAO-PS-OMMT-3 and PAO-PS-OMMT-5 are shown in Figure 11A–D and Figure 12A–D, respectively. As shown in Figure 11A, a deep and wide groove formed on the wear surface and can be associated with the effect of the presence of hard particles between the contact surfaces. Figure 12A further verified the existence of this worn morphology. It can be seen from Figure 11B that the grooves on the wear surface were shallow in depth and narrow in width compared with those in Figure 11A, suggesting that the addition of PS-OMMT-1 nanocomposite particles could improve the surface roughness and reduce the COF. A smooth wear surface with microgrooves and nanogrooves was observed for the PAO-PS-OMMT-3 sample, as shown in Figures 11C and 12C. However, the wear surface of the nanocomposites containing 5 wt % OMMT show deep scratch-like lines and coarse surfaces, which indicates that the plowing phenomenon occurred more severely on the surface compared to the composite containing 3 wt % OMMT. This result was due to the aggregation of the OMMT layers in the PS-OMMT-5 samples, which led to poor dispersion and caused three-body abrasion, reducing the lubrication effect of the nanocomposite particles. As shown in Figure 12, the wear scar diameters (WSDs) for the PAO, PAO-PS-OMMT-1, PAO-PS-OMMT-3 and PAO-PS-OMMT-5 samples were $958.14 \pm 47.91$ µm, $993.70 \pm 44.71$ µm, $929.00 \pm 32.51$ µm and $1600.00 \pm 62.40$ µm, respectively. This result revealed that the PS-OMMT-3 nanocomposite particles showed the best antiwear properties among all the types of nanocomposite particles in this study. PS-OMMT-3 particles with better exfoliation and MMT dispersion might roll better between two surfaces and reduce the abrasive effect of the nanocomposite particles. Furthermore, the PS-OMMT-3 nanocomposite particles might fill the microgrooves more effectively and form protective films more easily on the metal surfaces, reducing friction more than other samples. These results suggested that the PS-OMMT nanocomposite particles were effective friction reduction and antiwear materials and could find applications in drilling fluid lubrication.
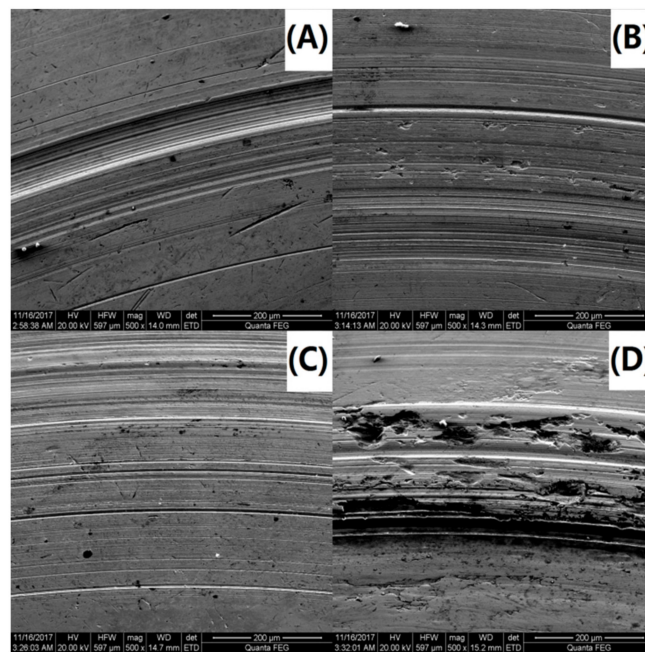
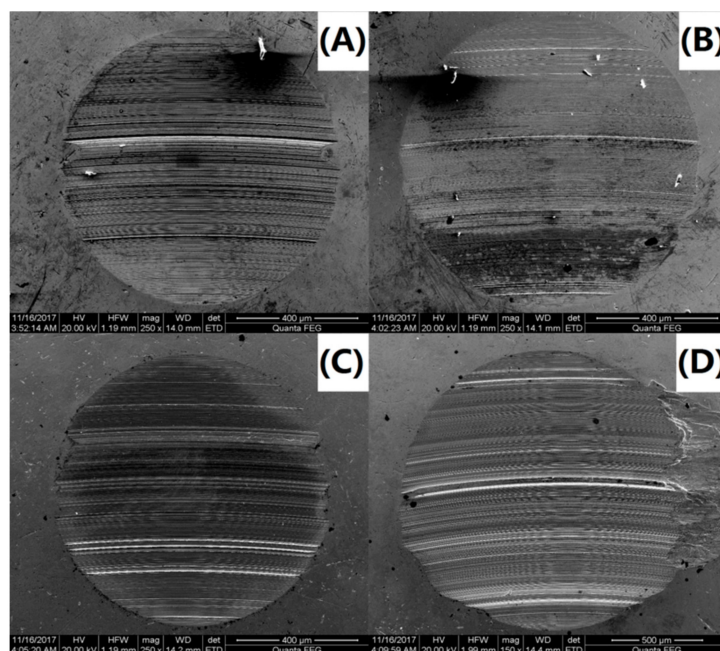**Figure 11.** SEM images of the upper ball of (**A**) PAO-PS, (**B**) PAO-PS-OMMT-1, (**C**) PAO-PS-OMMT-3 and (**D**) PAO-PS-OMMT-5.



**Figure 12.** SEM images of the lower ball of (**A**) PAO-PS, (**B**) PAO-PS-OMMT-1, (**C**) PAO-PS-OMMT-3 and (**D**) PAO-PS-OMMT-5.

## 4. Conclusions

PS-OMMT nanocomposite particles were successfully prepared using styrene and anionic surfactant-modified montmorillonite via emulsion polymerization, and the tribological properties of nanocomposite particles as additives to PAO were tested. FTIR, XRD, and TGA data confirmed the intercalation of SLS into the MMT interlayer spaces in acidic media. The average molecular weight and average particle size of the PS-OMMT nanocomposite particles were significantly decreased in

comparison with those of pure PS due to a hindering effect imposed by the OMMT layers. The XRD and TEM results for the PS-OMMT nanocomposites indicated the formation of exfoliated and intercalated structures and that the MMT layers were either partially embedded inside the PS particles or located on their surface. The TGA and DSC traces of the PS-OMMT nanocomposite particles revealed that they exhibited enhanced thermal decomposition stability and glass transition temperatures relative to pure PS. The PAO systems incorporating the nanocomposite particles exhibited higher friction reduction and antiwear properties compared with pure PAO. In addition, the nanocomposite particles at 3% OMMT-loading presented the best lubrication performance and kept a stable but very low COF level of 0.09. The proposed mechanism for all these improvements involved the effects of exfoliation and dispersion of the OMMT, as well as the stronger interaction between the OMMT and the PS matrix.

**Author Contributions:** Data curation, Q.D. and S.L.; Investigation, C.Y.; Methodology, Y.K.; Software, Y.Z.; Writing—original draft, C.Y.; Writing—review & editing, J.J. and X.H.

**Conflicts of Interest:** The authors declare no conflict of interest.

## References

1. Moraes, R.P.; Valera, T.S.; Pereira, A.M.C.; Demarquette, N.R.; Santos, A.M. Influence of the type of quaternary ammonium salt used in the organic treatment of montmorillonite on the properties of poly(styrene-co-butyl acrylate)/layered silicate nanocomposites prepared by in situminiemulsion polymerization. *J. Appl. Polym. Sci.* **2011**, *119*, 3658–3669. [CrossRef]

2. Kawasumi, M. The discovery of polymer-clay hybrids. *J. Polym. Sci. Part A Polym. Chem.* **2004**, *42*, 819–824. [CrossRef]

3. Zhang, G.; Ke, Y.; He, J.; Qin, M.; Shen, H.; Lu, S.; Xu, J. Effects of organo-modified montmorillonite on the tribology performance of bismaleimide-based nanocomposites. *Mater. Des.* **2015**, *86*, 138–145. [CrossRef]

4. EI-Sigeny, S.; Mohamed, S.K.; Taleb, M.F.A. Radiation synthesis and characterization of styrene/acrylic acid/organophilic montmorillonite hybrid nanocomposite for sorption of dyes from aqueous solutions. *Polym. Compos.* **2014**, *35*, 2353–2364. [CrossRef]

5. Huang, H.; Liu, H. Synthesis of the Raspberry-Like PS/PAN Particles with Anisotropic properties via seeded emulsion polymerization initiated by γ-Ray radiation. *J. Polym. Sci. Part A Polym. Chem.* **2010**, *48*, 5198–5205. [CrossRef]

6. Palanisamy, A. Water-blown polyurethane–clay nanocomposite foams from biopolyol—Effect of nanoclay on the properties. *Polym. Compos.* **2013**, *34*, 1306–1312. [CrossRef]

7. Chen, Y.N.; Chung, P.Y.; Yen, S.C. Conductivity and methanol permeability of sulfonated polystyrene membrane with dispersed montmorillonite nanoclay. *Polym. Compos.* **2012**, *33*, 2105–2113. [CrossRef]

8. Dawson, J.I.; Oreffo, R.O. Clay: New opportunities for tissue regeneration and biomaterial design. *Adv. Mater.* **2013**, *25*, 4069–4086. [CrossRef] [PubMed]

9. Wang, H.J.; Wang, H.Y.; Chen, K.; Song, Y.M.; Wei, Z.; Xue, M. The modification of lanthanum-exchanged montmorillonite with anionic surfactants to enhance the thermal stability of polyvinyl chloride. *J. Appl. Polym. Sci.* **2015**, *132*. [CrossRef]

10. Huang, J.C.; Zhu, Z.K.; Yin, J.; Qian, X.F.; Sun, Y.Y. Poly(etherimide)/montmorillonite nanocomposites prepared by melt intercalation: Morphology, solvent resistance properties and thermal properties. *Polymer* **2001**, *42*, 873–877. [CrossRef]

11. Ji, J.Q.; Ke, Y.C.; Pei, Y.; Zhang, G.L. Effects of highly exfoliated montmorillonite layers on the properties of clay reinforced terpolymer nanocomposite plugging microspheres. *J. Appl. Polym. Sci.* **2017**, *134*. [CrossRef]

12. Momani, B.; Sen, M.; Endoh, M.; Wang, X.L.; Koga, T.; Winter, H.H. Temperature dependent intercalation and self–exfoliation of clay/polymer nanocomposite. *Polymer* **2016**, *93*, 204–212. [CrossRef]

13. Soulestin, J.; Rashmi, B.J.; Bourbigot, S.; Lacrampe, M.F.; Krawczak, P. Mechanical and optical properties of polyamide 6/clay nanocomposite cast films: Influence of the degree of exfoliation. *Macromol. Mater. Eng.* **2012**, *297*, 444–454. [CrossRef]

14. Hwang, S.J.; Yong, L.J.; Lee, S.J. Properties of High-Impact Polystyrene/Organoclay Nanocomposites Synthesized via In Situ Polymerization. *J. Appl. Polym. Sci.* **2008**, *110*, 1141–1450. [CrossRef]

15. Liu, L.; Wei, S.L.; Lai, X.J. In situ synthesis and characterization of polypropylene/polyvinyl acetate-organophilic montmorillonite nanocomposite. *J. Appl. Polym. Sci.* **2012**, *124*, 4107–4113. [CrossRef]

16. Chen, G.M.; Liu, S.H.; Chen, S.J.; Qi, Z.N. FTIR spectra, thermal properties, and dispersibility of a polystyrene/montmorillonite nanocomposite. *Macromol. Chem. Phys.* **2001**, *202*, 1189–1193. [CrossRef]

17. Simons, R.; Qiao, G.G.; Powell, C.E.; Bateman, S.A. Effect of surfactant architecture on the properties of polystyrene-montmorillinite nanocomposites. *Langmuir* **2010**, *26*, 9023–9031. [CrossRef] [PubMed]

18. Zhu, J.; Morgan, A.B.; Lamelas, F.J.; Wilkie, C.A. Fire properties of polystyrene-clay nanocomposites. *Chem. Mater.* **2001**, *13*, 3774–3780. [CrossRef]

19. Zhang, Z.; Liao, L.; Xia, Z. Ultrasound-assisted preparation and characterization of anionic surfactants modified montmorillonites. *Appl. Clay. Sci.* **2010**, *50*, 576–581. [CrossRef]

20. Paiva, L.B.D.; Morales, A.R.; Diaz, F.R.V. Organoclays: Properties, preparation and applications. *Appl. Clay. Sci.* **2008**, *42*, 8–24. [CrossRef]

21. Alansi, A.M.; Alkayali, W.Z.; Al-Qunaibit, M.H.; Qahtan, T.F.; Saleh, T.A. Synthesis of exfoliated polystyrene/anionic clay MgAl-layered double hydroxide: Structural and thermal properties. *RSC Adv.* **2015**, *5*, 71441–71448. [CrossRef]

22. Zhu, L.; Guo, J.; Liu, P. Effects of length and organic modification of attapulgite nanorods on attapulgite/polystyrene nanocomposite via in-situ radical bulk polymerization. *Appl. Clay. Sci.* **2016**, *119*, 87–95. [CrossRef]

23. Ianchis, R.; Donescu, D.; Petcu, C.; Ghiurea, M.; Anghel, D.F.; Stanga, G.; Marcu, A. Surfactant-free emulsion polymerization of styrene in the presence of silylated montmorillonite. *Appl. Clay. Sci.* **2009**, *45*, 164–170. [CrossRef]

24. Qian, Z.; Zhou, H.; Xu, X.; Ding, Y.; Zhang, S.; Yang, M. Effect of the grafted silane on the dispersion and orientation of clay in polyethylene nanocomposites. *Polym. Compos.* **2009**, *30*, 1234–1242. [CrossRef]

25. Wang, L.; Wang, X.; Chen, Z.; Ma, P. Effect of doubly organo-modified vermiculite on the properties of vermiculite/polystyrene nanocomposites. *Appl. Clay. Sci.* **2013**, *75–76*, 74–81. [CrossRef]

26. Zhang, K.; Chen, H.; Chen, X.; Chen, Z.; Cui, Z.; Yang, B. Monodisperse silica-polymer core-shell microspheres via surface grafting and emulsion polymerization. *Macromol. Mater. Eng.* **2003**, *288*, 380–385. [CrossRef]

27. Li, H.; Yu, Y.; Yang, Y. Synthesis of exfoliated polystyrene/montmorillonite nanocomposite by emulsion polymerization using a zwitterion as the clay modifier. *Eur. Polym. J.* **2005**, *41*, 2016–2022. [CrossRef]

28. Wang, J.; Hu, Y.; Wang, S.; Chen, Z. Sonochemical one-directional growth of montmorillonite–polystyrene nanocomposite. *Ultrason. Sonochem.* **2005**, *12*, 165–168. [CrossRef] [PubMed]

29. Yang, W.T.; Ko, T.H.; Wang, S.C.; Shih, P.I.; Chang, M.J.; Jiang, G.J. Preparation of polystyrene/clay nanocomposite by suspension and emulsion polymerization. *Polym. Compos.* **2010**, *29*, 409–414. [CrossRef]

30. Yi, D.; Yang, H.; Zhao, M.; Huang, L.; Camino, G.; Frache, A.; Yang, R. A novel, low surface charge density, anionically modified montmorillonite for polymer nanocomposites. *RSC Adv.* **2017**, *7*, 5980–5988. [CrossRef]

31. Yang, L.; Ke, Y. Synthesis of polystyrene nanolatexes via emulsion polymerization using sodium dodecyl sulfonate as the emulsifier. *High Perform. Polym.* **2014**, *26*, 900–905. [CrossRef]

32. Piscitelli, F.; Posocco, P.; Toth, R.; Fermeglia, M.; Pricl, S.; Mensitieri, G.; Lavorgna, M. Sodium montmorillonite silylation: Unexpected effect of the aminosilane chain length. *J. Colloid. Interf. Sci.* **2010**, *351*, 108–115. [CrossRef] [PubMed]

33. Bhanvase, B.A.; Pinjari, D.V.; Gogate, P.R.; Sonawane, S.H.; Pandit, A.B. Synthesis of exfoliated poly(styrene-co-methyl methacrylate)/montmorillonite nanocomposite using ultrasound assisted in situ emulsion copolymerization. *Chem. Eng. J.* **2012**, *181–182*, 770–778. [CrossRef]

34. Ezquerro, C.S.; Ric, G.I.; Miñana, C.C.; Bermejo, J.S. Characterization of montmorillonites modified with organic divalent phosphonium cations. *Appl. Clay. Sci.* **2015**, *111*, 1–9. [CrossRef]

35. Faucheu, J.; Gauthier, C.; Chazeau, L.; Cavaille, J.Y.; Mellon, V.; Lami, E.B. Miniemulsion polymerization for synthesis of structured clay/polymer nanocomposites: Short review and recent advances. *Polymer* **2010**, *51*, 6–17. [CrossRef]

36. Wu, Y.; Zhang, J.; Zhao, H. Functional colloidal particles stabilized by layered silicate with hydrophilic face and hydrophobic polymer brushes. *J. Polym. Sci. Polym. Chem.* **2009**, *47*, 1535–1543. [CrossRef]

37. Hu, J.; Chen, M.; Wu, L. Organic-inorganic nanocomposites synthesized via miniemulsion polymerization. *Polym. Chem.* **2011**, *2*, 760–772. [CrossRef]

38. Greesh, N.; Sanderson, R.; Hartmann, P. Prepatation of polystyrene-clay nanocomposites via dispersion polymerization using oligomeric styrene-montmorillonite as stabilizer. *Polym. Int.* **2012**, *61*, 834–843. [CrossRef]

39. Patel, H.A.; Somani, R.S.; Bajaj, H.C.; Jasra, R.V. Preparation and characterization of phosphonium montmorillonite with enhanced thermal stability. *Appl. Clay. Sci.* **2007**, *35*, 194–200. [CrossRef]

40. Bee, S.L.; Abdullah, M.A.A.; Mamat, M.; Bee, S.T.; Sin, L.T.; Hui, D.; Rahmat, A.R. Characterization of silylated modified clay nanoparticles and its functionality in PMMA. *Compos. Part B Eng.* **2017**, *110*, 83–95. [CrossRef]

41. Periyayya, U.; Joo, K.H.; Hong, C.; Eun-Kyung, S.; Youn-Sik, L. Preparation of exfoliated high-impact polystyrene/MMT nanocomposites via in situ polymerization under controlling viscosity of the reaction medium. *Polym. Compos.* **2010**, *29*, 142–148.

42. Greesh, N.; Hartmann, P.C.; Cloete, V.; Sanderson, R.D. Impact of the clay organic modifier on the morphology of polymer–clay nanocomposites prepared by in situ free-radical polymerization in emulsion. *J. Polym. Sci. Polym. Chem.* **2008**, *46*, 3619–3628. [CrossRef]

43. Dong, Z.; Liu, Z.; Zhang, J.; Han, B.; Sun, D.; Wang, Y.; Huang, Y.J. Synthesis of montmorillonite/polystyrene nanocomposites in supercritical carbon dioxide. *Appl. Polym. Sci.* **2004**, *94*, 1194–1197. [CrossRef]

44. Chen, S.; Lu, X.; Zhang, Z.; Wang, T.; Pan, F. Preparation and characterization of poly (methyl methacrylate)/reactive montmorillonite nanocomposites. *Polym. Compos.* **2016**, *37*, 2396–2403. [CrossRef]

45. Fu, X.; Qutubuddin, S. Synthesis of polystyrene–clay nanocomposites. *Mater. Lett.* **2000**, *42*, 12–15. [CrossRef]